

Aberration compensation of optical tweezers for single-atom array

Jia-Yi Hou(侯嘉毅), Yu Jia(贾玉), Wen-Jun Xiao(夏文君), Yu Liu(刘宇), Zhi-Quan Shi(石志全), Ying-Jie Bai(白英杰), Kong-Rui Ma(马孔睿), Zhuo Fu(付卓)

Citation: Chin. Phys. B.2026. 35(**8**): 084201. DOI: 10.1088/1674-1056/ae2d35
http://cpb.iphy.ac.cn; http://iopscience.iop.org/cpb

What follows is a list of articles you may be interested in

Design of a compact wide-field-of-view infrared imager based on wavefront coding

Chonghui Zhu(朱崇辉), Jiaqian Yu(于佳倩), and Jingang Cui(崔金刚)
Chin. Phys. B, 2026, 35 (**2**): 024202. DOI: 10.1088/1674-1056/adf03f

Controlled propagation and particle manipulation of off-axis-rotating elliptical Gaussian beams in strong nonlocal media

Rong-Quan Chen(陈荣泉), Rui-Lin Xiao(肖瑞林), Wei Wang(王伟), Xi-Xi Chu(储茜茜), Yu-Qing Song(宋雨晴), Xu-Dong Hu(胡旭东), and Ming Chen(陈明)
Chin. Phys. B, 2025, 34 (**3**): 034205. DOI: 10.1088/1674-1056/ada9dd

Light-field modulation and optimization near metal nanostructures utilizing spatial light modulators

Zini Cao(曹子倪), Hai Lin(林海), Yuqing Cheng(程宇清), Yixuan Xu(徐艺轩), Qihuang Gong(龚旗煌), and Guowei Lü(吕国伟)
Chin. Phys. B, 2024, 33 (**10**): 104201. DOI: 10.1088/1674-1056/ad6555

Design of an all-dielectric long-wave infrared wide-angle metalens

Ning Zhang(张宁), Qingzhi Li(李青芝), Jun Chen(陈骏), Feng Tang(唐烽),Jingjun Wu(伍景军), Xin Ye(叶鑫), and Liming Yang(杨李茗)
Chin. Phys. B, 2022, 31 (**7**): 074212. DOI: 10.1088/1674-1056/ac4026

Wavefront evolution of the signal beam in Ti: sapphire chirped pulse amplifier

Zhen Guo(郭震), Lianghong Yu(於亮红), Wenqi Li(李文启), Zebiao Gan(甘泽彪), Xiaoyan Liang(梁晓燕)
Chin. Phys. B, 2019, 28 (**1**): 014203. DOI: 10.1088/1674-1056/28/1/014203

SPECIAL TOPIC — Quantum frontiers with Rydberg atoms

Aberration compensation of optical tweezers for single-atom array

Jia-Yi Hou(侯嘉毅)[1], Yu Jia(贾玉)[2], Wen-Jun Xiao(夏文君)[1], Yu Liu(刘宇)[1], Zhi-Quan Shi(石志全)[1], Ying-Jie Bai(白英杰)[1], Kong-Rui Ma(马孔睿)[1], and Zhuo Fu(付卓)[1,†]

[1] *CAS Cold Atom Technology (Wuhan) Co., Ltd., Wuhan* 430074, *China*
[2] *Mobile (Suzhou) Software Technology Company Limited, Suzhou* 215163, *China*

(Received 20 October 2025; revised manuscript received 9 December 2025; accepted manuscript online 16 December 2025)

High-precision preparation of holographic optical tweezers, which is a critical requirement for neutral atom quantum computing platforms, faces the challenge of system aberrations that degrade trap performance. In this paper, we propose a simple and efficient aberration correction algorithm for wavefront-sensorless optical systems, based on correcting the relative lateral shift of diffracted light across spatial regions. Applied to a cold atomic system, this technique demonstrates active correction of aberrations up to several wavelengths, reducing them to a peak-to-valley difference of $0.19(3)\lambda$. The diffraction spot quality and optical trap depth are significantly improved after aberration correction. Combined with subsequent array optimization, the technique enables the generation of uniform optical trap arrays with enhanced atom-loading efficiency. The method requires no prior wavefront information or additional hardware, utilizing only an SLM and a standard CCD camera. Its computational efficiency and hardware simplicity make it broadly applicable to fields such as laser lithography and microscopy.

Keywords: wavefront aberration, spatial light modulator, optical tweezer, single-atom array

PACS: 42.15.Dp, 42.15.Fr, 37.10.Gh, 03.67.Lx

DOI: 10.1088/1674-1056/ae2d35 **CSTR:** 32038.14.CPB.ae2d35

1. Introduction

Over the past decades, holographic optical tweezers, which provide optical forces through focused laser beams, have been widely used in life sciences and atomic and molecular physics.[1–3] When combined with laser cooling,[4] holographic optical tweezers can trap single atoms by leveraging the collisional blockade effect.[5] Neutral atom arrays have emerged as a promising platform for quantum metrology,[2,3] many-body simulation,[6–9] and quantum computation.[10–12] Optical tweezer arrays for cold-atom control can now scale to thousands of sites,[13–18] imposing demanding requirements on laser precision. However, wavefront aberrations inevitably compromise beam quality, degrading both atom-loading efficiency and quantum gate fidelity.[10,11]

Wavefront aberrations typically originate from imperfections in active electro-optic devices for generating optical tweezer arrays, suboptimal optical components, or mismatches within the optical system.[19] In recent decades, aberration compensation has presented a significant challenge and has garnered substantial attention across various fields, notably in astronomy,[20] optical tweezers,[21] and microscopy.[22] Typically, aberrations are measured either directly using Shack–Hartmann (SH) wavefront sensors[21,23,24] or indirectly through phase-shifting interferometry (PSI),[22,25,26] and are then corrected using spatial light modulators, deformable mirrors, digital micromirror devices, and so on. Implementing SH sensors is relatively straightforward; however, their integration into an existing optical path requires the insertion of a physical microlens array. This can introduce additional optical surfaces, potential misalignment, and further aberrations, which is undesirable in systems where stability and optical simplicity are paramount, such as cold-atom experiments. In principle, phase-shifting interferometry (PSI) can correct large aberrations with high accuracy.[19,25,26] However, its practical application often requires time-consuming, fine phase-stepping scans and stable fringe detection. This process becomes increasingly challenging and inefficient in the presence of large initial wavefront errors. Several aberration compensation methods based on machine learning have been proposed.[27–30] However, these approaches often necessitate extensive training datasets and substantial computational resources.

In this work, we propose a simple and efficient wavefront-sensorless aberration correction scheme that overcomes several limitations of existing methods. Our approach utilizes only the spatial light modulator (SLM) already present in typical holographic optical tweezer systems and a standard charge-coupled device (CCD) camera, without requiring additional wavefront sensing hardware. By partitioning the SLM into a grid of patches and measuring the relative lateral shifts of corresponding diffracted spots, we directly extract local phase gradients and reconstruct a global compen-

[†]Corresponding author. E-mail: fuzhuo@cascoldatom.com

© 2026 Chinese Physical Society and IOP Publishing Ltd. All rights, including for text and data mining, AI training, and similar technologies, are reserved.

sation phase map through iterative smoothing and integration. This method eliminates the need for physical wavefront sensors, avoids time-consuming phase-stepping scans, and operates effectively even under large initial aberrations — key advantages over conventional SH and PSI techniques.

In the following, we first describe the experimental setup and the principle of the correction process (Section 2). We then present the experimental validation of the method, including wavefront reconstruction results, diffraction spot improvements, and optical trap array performance before and after aberration correction (Section 3). Finally, we discuss the broader implications of the technique and its potential applications beyond cold-atom systems (Section 4). Our experimental demonstration in a cold-atom system shows active correction of aberrations up to several wavelengths, reducing the peak-to-valley wavefront error from $2.6(3)\lambda$ to $0.19(3)\lambda$, with significant improvements in diffraction spot quality and optical trap depth. The method's hardware simplicity, computational efficiency, and lack of requirement for prior wavefront information make it promising not only for neutral-atom quantum platforms but also for broader applications in fields such as laser lithography and microscopy.

2. Experimental setup and principle of correction process

Figure 1 illustrates our cold-atom experimental setup for aberration correction. Trapping light from an 830-nm fiber laser is collimated, expanded, and directed onto a computer-controlled spatial light modulator (SLM; Hamamatsu X15223). The phase-modulated beam propagates through relay optics and a high numerical aperture objective (NA = 0.55), focusing to about 1 μm waist within the vacuum chamber. The SLM is tilted by 8° relative to the optical axis, features a pixel size of 12.5 μm, and contains 1272×1024 pixels. A magneto-optical trap (MOT) prepares ^{87}Rb clouds at 50 μK centered on the SLM-conjugate image plane. Atoms are loaded into optical traps (typical depth $U_0 = k_B \times 1$ mK) and cooled to 7 μK via 20 ms polarization gradient cooling (PGC). Single-atom fluorescence at 780 nm is detected by a scientific complementary metal-oxide-semiconductor (sCMOS) camera (Dhyana-400BSI-V3) after spectral separation using a dichroic mirror (DM). Transmitted trapping light is imaged onto an 8-bit CCD for diffraction-spot diagnostics. SLM surface aberrations are characterized by analyzing CCD images of test phase patterns, enabling subsequent wavefront correction.

Before implementing aberration compensation, the Fourier correspondence relationship was first verified. The input field on the SLM has a Fourier correspondence relationship with the image plane inside the vacuum chamber, and it also corresponds to the Fourier transform of the light field distribution that reaches the CCD plane after being amplified by the 4f lens group. Under ideal conditions, the light field on the CCD plane is given by

$$E_{(u,v)} = \frac{1}{N_x N_y} \sum_{x=0}^{N_x-1} \sum_{y=0}^{N_y-1} A_{(x,y)} \, \mathrm{e}^{\mathrm{i}\varphi_{(x,y)}} \times \mathrm{e}^{-\mathrm{i}\frac{2\pi}{N_x} k_{x_0}(u-u_0)x - \mathrm{i}\frac{2\pi}{N_y} k_{y_0}(v-v_0)y}, \quad (1)$$

where N_x and N_y denote the total pixel count along the horizontal and vertical dimensions of the SLM's active area, $A(x,y)$ and $\varphi(x,y)$ represent the amplitude and phase of the incident field at physical pixel coordinates (x,y), u_0 and v_0 indicate the center coordinates of the diffraction pattern imaged on the CCD plane with no phase modulation applied to the SLM, and k_{x_0} and k_{y_0} are the proportional magnification coefficients related to the focal length of the equivalent focusing lens of the system. These coefficients depend on factors such as the laser wavelength, the magnification of the emitted light, the pixel pitch of the SLM, and the pixel pitch of the CCD.

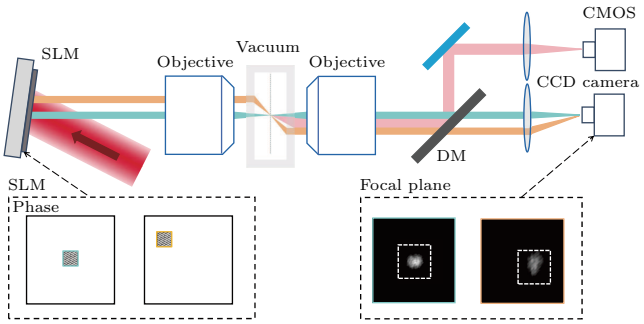


Fig. 1. Schematic of the experimental setup and the block diagram of the aberration correction process. Trap light at a wavelength of 830 nm is reflected by a spatial light modulator (SLM), which modulates the light phase using the calculated pattern. The laser is collimated and then passes through a series of lenses and a high-resolution objective before entering the vacuum chamber. Subsequently, the light passes through a dichroic mirror (DM) and is observed with a CCD. The DM separates the fluorescence from the trapping light, which is then detected by a CMOS camera. Our aberration compensation method involves loading blazed gratings on individual patches of the SLM and using the CCD to measure the relative position offsets of the corresponding light fields.

When applying a computer-generated hologram (CGH) with a global phase gradient across the SLM's active area as $\varphi = 2\pi x/T_x + 2\pi y/T_y$, the spatial positions of first-order diffraction spots on the CCD plane exhibit a linear dependence on T_x and T_y. The coefficients k_{x0} and k_{y0} are directly measurable through linear parameter scanning. We employ the SLM to impart a phase gradient onto a localized segment of the outgoing wavefront (as illustrated in the left inset of Fig. 1). This allows us to isolate and extract a small portion of the light field from the SLM, distinct from the region where the diffracted light field generated by the remaining SLM area is mapped on the CCD plane. For sufficiently small patch sizes, the amplitude and phase of the optical field can be reasonably approximated as coherent. The ideal center (u_0, v_0) of this light-field

portion is calculable via Eq. (1). However, as illustrated in the right inset of Fig. 1, aberrations and the intensity gradient at the incident light spot's edge distort the observed diffraction field, preventing accurate localization of the main maximum. We therefore compute an approximate center (u_c, v_c) using a weighted centroid algorithm within an $N_H \times N_H$ region centered on (u_0, v_0), given by

$$u_c = \frac{\sum_{i=0}^{N_H^2-1} u_i^*(A_i - A_b)}{\sum_{i=0}^{N_H^2-1}(A_i - A_b)},\ v_c = \frac{\sum_{i=0}^{N_H^2-1} v_i^*(A_i - A_b)}{\sum_{i=0}^{N_H^2-1}(A_i - A_b)}, \quad (2)$$

where u_i^* and v_i^* denote the horizontal and vertical coordinates of the i-th pixel, respectively, while A_i represents the fluorescence intensity at that point. A_b denotes the residual average light field intensity of the zeroth-order diffraction within this region. Here, the weighting function is simply the intensity above background, i.e., $w_i = A_i - A_b$. Then, we apply appropriate phase gradients with periods (T_{xi}, T_{yi}) in this patch to correct the detected shifts iteratively until the center overlaps with the ideal one.

We use square patches of side length L pixels which are centered at SLM coordinates (x_i, y_i). These patches are positioned on an $M \times M$ sampling grid with spacing d pixels between adjacent grid points. The patch size L is optimized to balance signal-to-noise ratio with spatial distinguishability of different regions. The grid spacing d should be smaller than L to ensure that the patches overlap for better accuracy, but not too small to incur excessive scanning time. By sequentially loading patch-based computer-generated holograms (CGHs) across the SLM and computing the observed diffraction-field offsets on the CCD, we determine the required phase gradient compensation for each patch in the $M \times M$ grid. The phase gradients in overlapping regions are averaged over all contributing patches.

After determining the phase gradient compensation required for each region, we construct a global aberration compensation phase map for the SLM plane by integrating the $M \times M$ grid data through iterative smoothing operations. Here, (X_{ij}, Y_{ij}) denotes the horizontal and vertical phase gradient periods for compensation at grid position (i, j), while $\varphi_{i,j}$ represents the average phase offset of the corresponding patch. The accumulated phase difference between orthogonally adjacent patches is expressed as

$$\begin{aligned} \varphi_{i+1,j} - \varphi_{i,j} &= \frac{\pi d}{X_{i+1,j}} + \frac{\pi d}{X_{i,j}}, \\ \varphi_{i,j+1} - \varphi_{i,j} &= \frac{\pi d}{Y_{i,j+1}} + \frac{\pi d}{Y_{i,j}}. \end{aligned} \quad (3)$$

To circumvent over-constraint issues from full-phase utilization, we designate the grid center as the reference point and first compute column-wise mean phase offsets through inter-column phase differences; these values subsequently serve as references to determine row-wise mean phase offsets via inter-row phase differences. By integrating all patches' mean phase offsets ψ_{ij} and phase gradient parameters (X_{ij}, Y_{ij}) with normalization, we reconstruct the global aberration compensation phase map, which represents the system's comprehensive aberration profile.

In summary, the aberration correction is implemented by dividing the SLM into a grid of patches, sequentially measuring the relative diffraction spot displacements to ascertain local phase gradients, and reconstructing a global compensation phase map via iterative smoothing and integration. This approach, which directly utilizes relative diffraction shifts, is computationally straightforward and inherently more efficient than phase-shifting interferometry (PSI). By eliminating the time-intensive phase-shifting scans and fringe analysis required by PSI, our approach achieves a comparable correction accuracy at a speed that is approximately an order of magnitude greater.

The core principle of our correction method relies on the linear, shift-invariant geometric-optical relationship between the phase gradient applied on the SLM and the resulting lateral displacement of the diffracted spot on the CCD (as implied by Eq. (1)). This necessitates that the imaging system (including the objective, relay lenses, and the CCD camera) provides a faithful linear mapping within the field of view. Furthermore, optical components such as vacuum chamber windows should not introduce severe scattering or distortion that could corrupt the centroid measurement of the diffraction spots. In practice, mild field distortions can often be accommodated by performing the calibration within the region of interest used for trapping. However, systems with strong spatial nonlinearities may require more advanced modeling for accurate wavefront reconstruction.

3. Results and discussion

Through empirical evaluation, we determined the patch size $L = 64$, a choice that effectively ensures that the intensity of the background zero-order diffraction light is roughly 20 times weaker than that of the strongest optical field section intercepted by the patch. We applied the same phase gradient to distinct patches across the 45×45 sampling grid with $d = 16$. In order to capture the relative displacement of the cropped optical field on the CCD with respect to the ideal center in the X and Y directions, a series of measurements were conducted, and the outcomes are presented in Figs. 2(a) and 2(b).

Leveraging the established linear correlation between phase gradient and CCD optical field shift, we performed a continuous smoothing process to derive the corrected phase map and applied the necessary compensation. This process

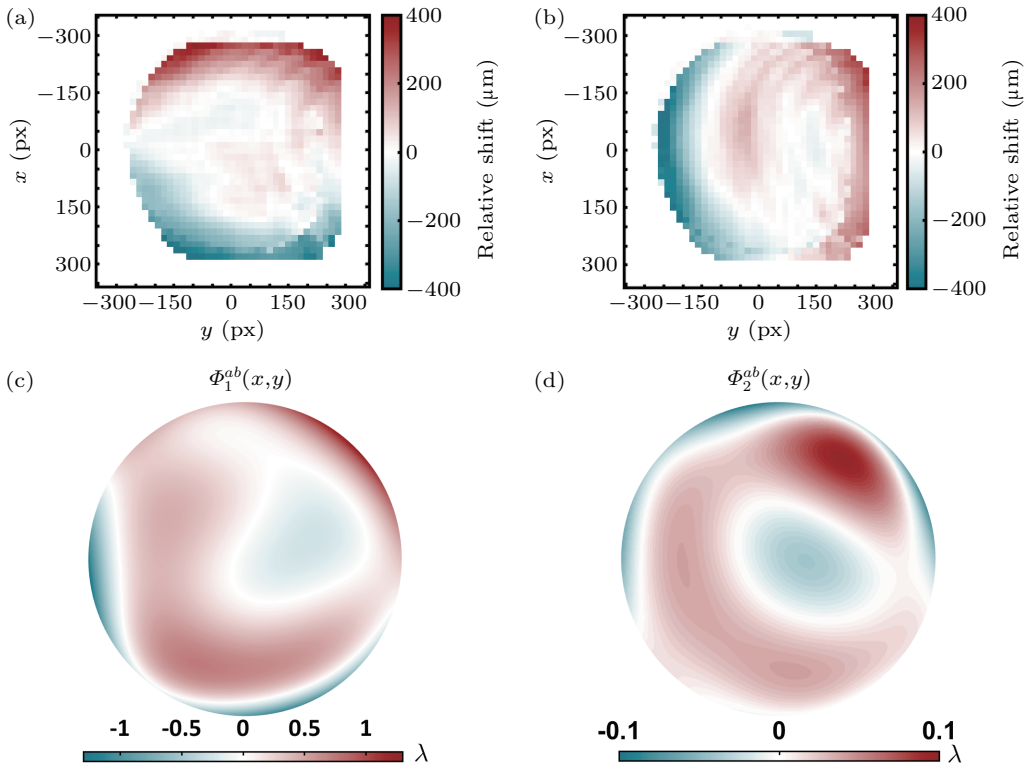


Fig. 2. Reconstruction of the aberrated wavefront. (a) and (b) illustrate the relative shift of the cropped optical field on the CCD with respect to the ideal center in the X and Y directions, respectively. These shifts were measured by applying a consistent phase gradient to individual patches across a 45×45 sampling grid, which has a grid spacing of 16 pixels. (c) presents the phase map, from which piston and tilt components have been removed, reconstructed by leveraging the linear relationship between phase gradient and optical field shift on the CCD. (d) shows the measured residual aberration map, also with piston and tilt components excluded, after performing three iterations of a smoothing process until the residual wavefront error stabilized.

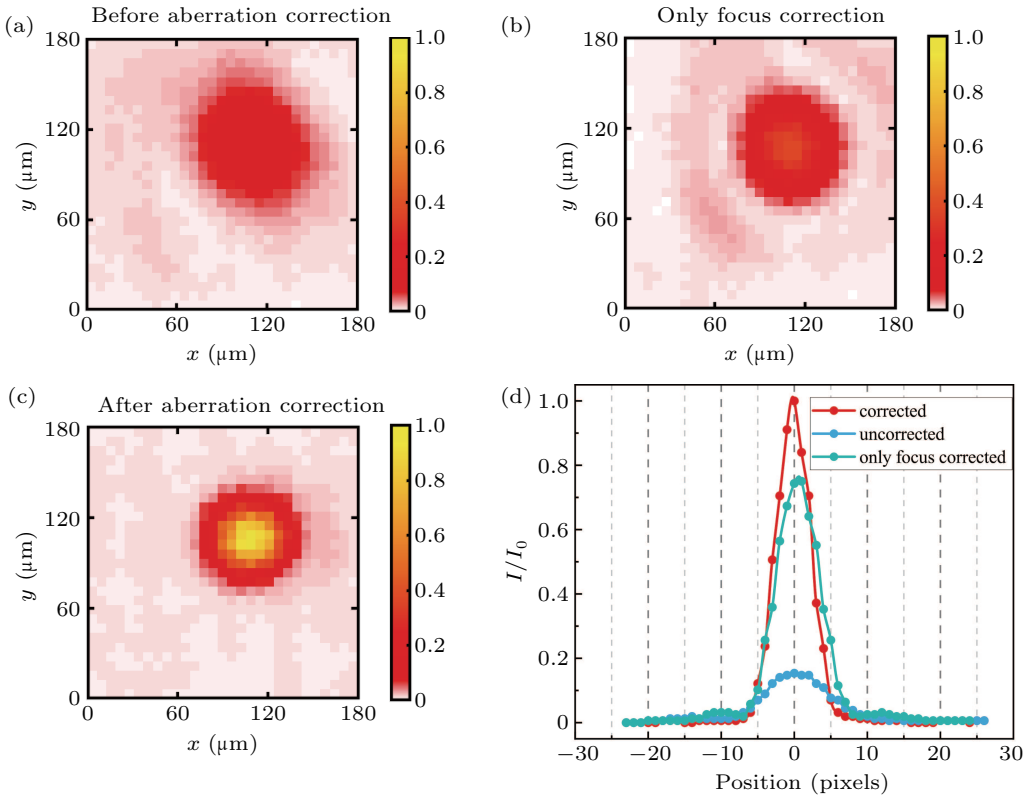


Fig. 3. Comparison of the diffraction light field before and after aberration correction with different forms of computer-generated holograms (CGH) loaded. (a), (b), and (c) show the intensity distribution of the first-order diffraction spot under three conditions: without aberration correction, with focus correction only, and with full aberration correction, respectively. (d) presents a comparison of the intensity profiles in the radial direction for the three conditions, with the blue line representing no correction, the green line representing focus correction only, and the red line representing full aberration correction. Note that each pixel corresponds to 6 μm.

was iterated three times, with iterations terminating when the residual wavefront error stabilized between consecutive cycles, indicating algorithmic convergence. To quantify the efficacy of the aberration correction, we decomposed the phase maps of both the fully compensated aberration and optimized residual system aberrations into Zernike coefficients. The resulting aberrations after excluding tilt and defocus terms are presented in Figs. 2(c) and 2(d). Quantitatively, the measured wavefront error corresponds to a peak-to-valley deviation of $2.6(3)\lambda$. Following three correction iterations, the residual aberration is reduced to a peak-to-valley deviation of $0.19(3)\lambda$.

To directly visualize the improvement in focusing performance achieved by the aberration correction, we compare the intensity profiles of the first-order diffraction spot under three conditions. Figure 3 illustrates the intensity distribution of the first-order diffraction spot under three scenarios: without aberration correction, with focus correction only, and with full aberration correction. Prior to aberration compensation, adjusting the focal length enhances the light intensity by 4.9 times. However, after complete aberration compensation, the intensity further increases to 6.4 times the original intensity. Additionally, the full width at half maximum (FWHM) reduces from 5.5 pixels (equivalent to 34.5 μm) to 4.69 pixels (equivalent to 28.14 μm).

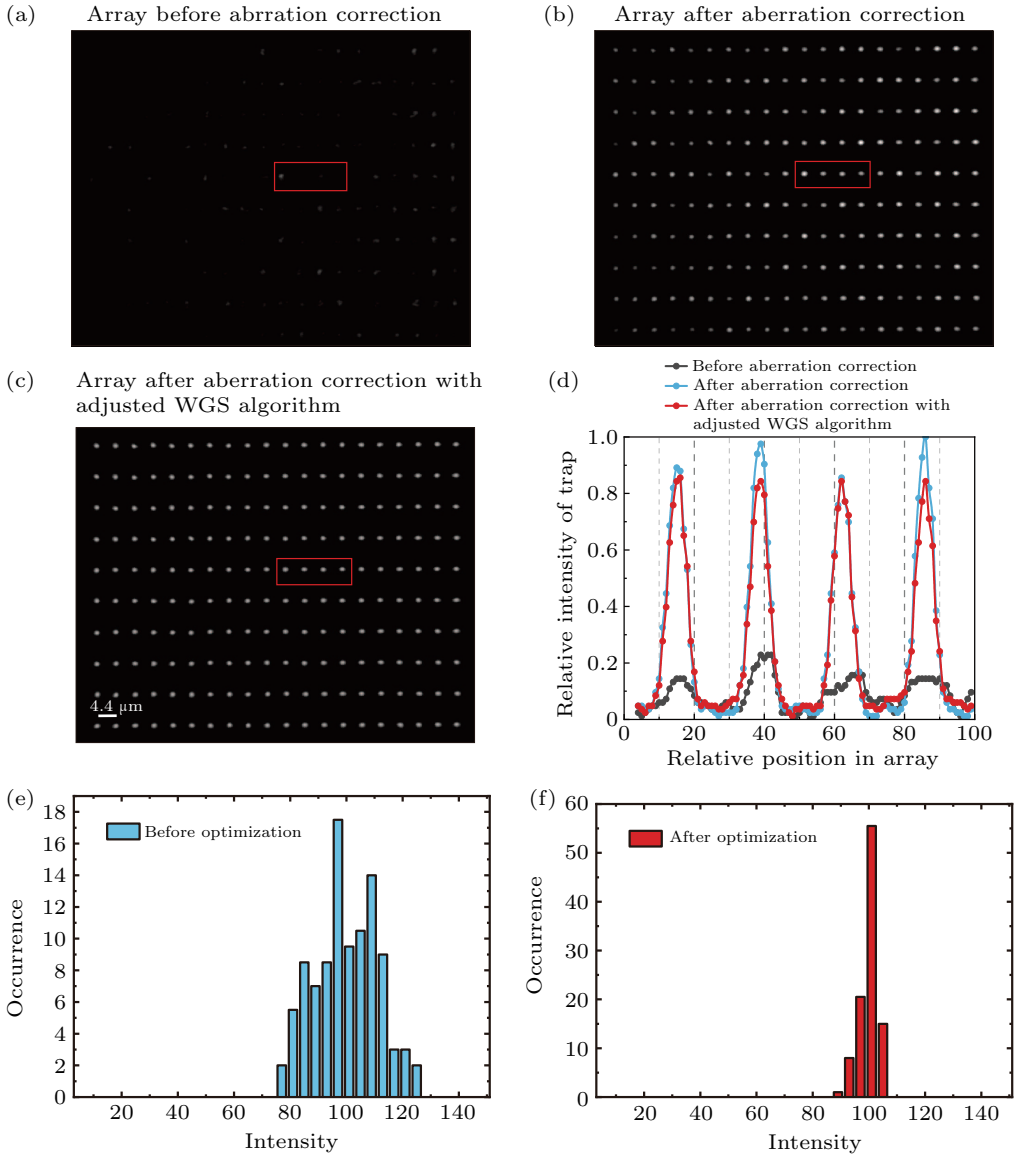


Fig. 4. Effect of the optical trap array after aberration correction and uniformity optimization. (a) The array on the CCD before aberration correction. (b) The array after aberration correction, showing a nearly five-fold enhancement in trap depth but with significant non-uniformity. (c) Optimized array image achieved by adjusting weights in the WGS algorithm based on the photon count from a CCD-imaged tweezers camera, reducing the root-mean-square (RMS) variation in trap depths from 11% to 3%. (d) Intensity profiles within the red-circled regions of (a), (b), and (c), comparing conditions without correction (black curve), with aberration correction only (blue curve), and with both aberration correction and uniformity optimization (red curve). (e) Histogram of trap depth before uniformity optimization. (The average intensity of all traps is normalized to 100.) (f) Histogram of trap depth after uniformity optimization. Note that all arrays were generated with the same calculated phase ϕ, and the laser power and CCD camera exposure time were kept constant across all cases.

While the enhanced diffraction spot confirms the optical system's improved focusing capability, the ultimate requirement for atom trapping is a uniform array of such spots. Consequently, we investigate the effect of aberration correction on a full tweezer array, as shown in Fig. 4. To achieve the desired intensity distribution at the image plane within the vacuum chamber, we employ the weighted Gerchberg–Saxton (WGS) algorithm[31] to compute the computer-generated hologram (CGH) for loading. Specifically, we generate a 20×10 array with a transverse spacing of 4.4 μm and a longitudinal spacing of 8.8 μm. Figures 4(a) and 4(b) depict the array images on the CCD before and after aberration correction, respectively. The comparison indicates that aberration correction can enhance the trap depth by nearly a factor of 5. However, the trap depth in the array shown in Fig. 4(b) exhibits significant non-uniformity. This is attributed to the omission of diffraction efficiency effects when generating the CGH using the WGS algorithm. As shown in Fig. 4(e), we observe a root-mean-square (RMS) variation of 11% in the trap depths (with minimum and maximum values of 75 and 126, respectively, and the average intensity of all traps normalized to 100). To address this, we adjust the weights in the WGS algorithm based on the photon count from a CCD-imaged tweezers camera, a method previously demonstrated for smaller arrays.[32] The optimized array image is presented in Fig. 4(f), where the trap depth variation is reduced to an RMS of 3%.

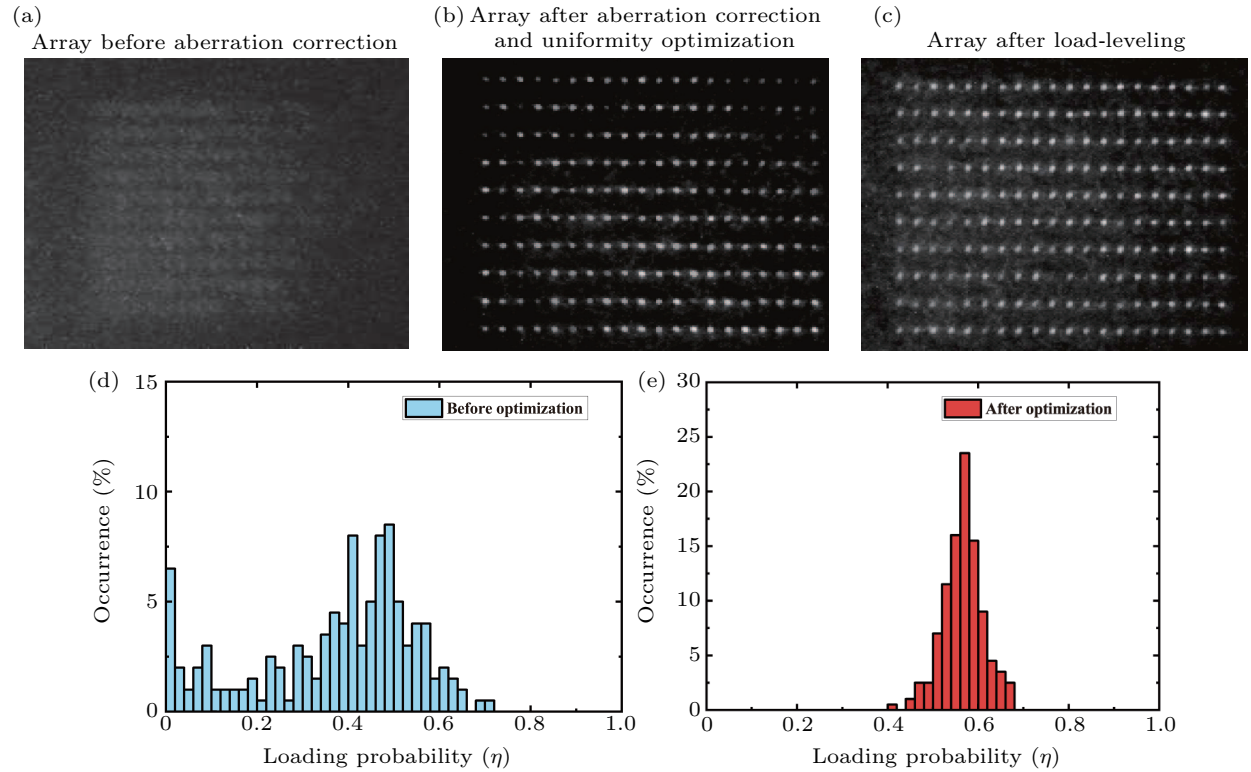


Fig. 5. Effect of aberration correction, uniformity optimization, and load-leveling on the 20×10 optical trap array. (a) Averaged fluorescence image (500 shots) of the array before aberration correction or uniformity optimization. The signal is completely defocused, preventing reliable identification of atoms at individual sites. (b) Averaged fluorescence image after aberration correction and uniformity optimization. Atoms are clearly resolved at all sites, but loading remains non-uniform. (c) Averaged fluorescence image after further *in-situ* load-leveling based on atom loading probability feedback. (d) Spatial distribution of loading probabilities corresponding to the state in (b). (e) Spatial distribution of loading probabilities corresponding to the state in (c), showing significantly enhanced uniformity with all traps exceeding 40% loading probability.

To further validate the performance improvement of the optical trap array achieved through aberration correction combined with uniformity optimization, we compared its atom-loading capability before and after this process, as shown in Fig. 5. Figure 5(a) displays the averaged fluorescence image (500 shots) of the array before aberration correction or uniformity optimization. The fluorescence signal is completely defocused, preventing reliable identification of loaded atoms at individual sites. This severe blurring directly demonstrates the detrimental impact of the initial wavefront aberrations on the imaging fidelity. After applying both aberration correction and uniformity optimization, the trapping potential and imaging quality were significantly restored. The corresponding averaged fluorescence image in Fig. 5(b) now shows clearly resolved atoms at all array sites. However, the spatial distribution of the atom loading probability remains non-uniform, as quantified in Fig. 5(d). This indicates that while gross aberrations are corrected, subtle variations in individual trap profiles or residual imaging path imperfections can still lead to inhomogeneous loading. Subsequently, to achieve uniform loading across the array, we implemented the *in-situ* load-leveling technique.[33] We analyzed the correlation between the site-resolved loading probability and the average power, and iteratively adjusted the intensity weights in the WGS algorithm

accordingly. The results after this final optimization are presented in Figs. 5(c) and 5(e). They demonstrate a significant enhancement in loading uniformity, with the loading probability for all traps exceeding 40%.

4. Conclusion

In summary, we have experimentally demonstrated and applied a wavefront-sensorless phase-gradient correction method to compensate for aberrations in a cold-atom optical tweezer system. The aberration was reduced from an initial peak-to-valley (PV) value of $2.6(3)\lambda$ to $0.19(3)\lambda$, leading to a significant enhancement in both the quality of the diffraction spot and the depth of the optical traps.

The practical significance of our method lies in its hardware simplicity, operational efficiency, and programmable flexibility. By utilizing only the existing SLM and a standard CCD camera, it offers a truly *in-situ* and non-invasive correction capability. Crucially, parameters such as patch size, grid layout, and reference points are fully software-definable, enabling adaptive sampling tailored to the specific aberration structure of a system — a degree of reconfigurability not afforded by fixed-geometry Shack–Hartmann sensors. Furthermore, the method operates without the time-consuming phase-stepping scans required by phase-shifting interferometry (PSI), enabling faster convergence even with large initial aberrations. These attributes make it particularly suitable as an efficient pre-correction step, rapidly establishing a high-quality wavefront baseline necessary for subsequent, more demanding optimization procedures.

Our results also elucidate the nature and impact of the corrected aberrations, which constitute a composite error from multiple sources along the optical path. The most direct evidence of correction efficacy is seen in the imaging plane: prior to correction, the atomic array was severely defocused and indistinguishable, whereas after correction, individual atom sites became clearly resolvable. This dramatic improvement in imaging fidelity confirms that aberrations in the tweezer generation path (from the SLM to the atom plane) were a dominant factor limiting system performance. The subsequent need for load-leveling to achieve uniform atom loading, however, indicates that residual effects — such as site-specific trap variations or imperfections in the separate imaging path — merit further attention for achieving optimal array uniformity.

A comprehensive solution may involve integrating our pre-correction method with finer, *in-situ* optimization techniques. Promising directions include combining phase-shifting interferometry with atomic fluorescence feedback[19] or employing SLM-based shaping to individually optimize trap profiles.[34] Our aberration pre-correction method effectively meets the stringent initial wavefront requirements of these advanced techniques, thereby enabling their practical application.

The method is general, relying on the fundamental linear relationship between SLM phase gradient and CCD spot displacement within a well-corrected field of view. It is therefore directly applicable to the development and optimization of other advanced cold-atom platforms, such as programmable optical tweezer arrays based on strontium atoms for quantum simulation and metrology.[35] In systems exhibiting strong spatial nonlinearity, the reconstructed phase map may depend on the choice of reference point, a factor noted in our reconstruction process. In such cases, our method can serve as a valuable diagnostic starting point. By measuring the phase compensation maps derived from different reference points, it provides initial data that could inform and facilitate more advanced system modeling for full characterization.

Therefore, our work not only presents a practical tool for cold-atom systems but also establishes a general paradigm for wavefront-sensorless aberration correction in applications where hardware simplicity and operational speed are critical. Its computational efficiency and lack of need for prior wavefront information suggest broader applicability beyond optical tweezers, for example in laser lithography and microscopy, where it can serve as a faster and more robust alternative to PSI for initial aberration compensation and system characterization.[22,36]

Acknowledgments

Project supported by the Technology Achievement Transformation Project of Wuhan (Grant No. 2024030803010168) and the Major Program (JD) of Hubei Province (Grant No. 2023BAA020). Part of the results was accomplished based on the Hun-Dun Quantum Experimental Platform of China Mobile.

References

[1] Kaufman A M and Ni K K 2021 *Nat. Phys.* **17** 1324
[2] Madjarov I S, Cooper A, Shaw A L, Covey J P, Schkolnik V, Yoon T H, Williams J R and Endres M 2019 *Phys. Rev. X* **9** 041052
[3] Norcia M A, Young A W, Eckner W J, Oelker E, Ye J and Kaufman A M 2019 *Science* **366** 93
[4] Chu S, Hollberg L, Bjorkholm J E, Cable A and Ashkin A 1985 *Phys. Rev. Let.* **55** 48
[5] Schlosser N, Reymond G and Grangier P 2002 *Phys. Rev. Let.* **89** 023005
[6] Browaeys A 2020 *Nat. Phys.* **16** 132
[7] Scholl P, Schuler M, Williams H J, Eberharter A A, Barredo D, Schymik K N, Lienhard V, Henry L P, Lang T C, Lahaye T, Läuchli A M and Browaeys A 2021 *Nature* **595** 233
[8] Ebadi S, Wang T T, Levine H, Keesling A, Semeghini G, Omran A, Bluvstein D, Samajdar R, Pichler H, Ho W W, Choi S, Sachdev S, Greiner M, Vuletić V and Lukin M D 2021 *Nature* **595** 227
[9] Altman E, Brown K R, Carleo G, *et al.* 2021 *PRX Quantum* **2** 017003
[10] Bluvstein D, Levine H, Semeghini G, Wang T T, Ebadi S, Kalinowski M, Keesling A, Maskara N, Pichler H, Greiner M, Vuletić V and Lukin M D 2022 *Nature* **604** 451

[11] Graham T M, Song Y, Scott J, *et al.* 2022 *Nature* **604** 457
[12] Bluvstein D, Evered S J, Geim A A, *et al.* 2024 *Nature* **626** 58
[13] Gyger F, Ammenwerth M, Tao R, Timme H, Snigirev S, Bloch I and Zeiher J 2024 *Phys. Rev. Res.* **6** 033104
[14] Pause L, Sturm L, Mittenbühler M, Amann S, Preuschoff T, Schäffner D, Schlosser M and Birkl G 2024 *Optica* **11** 222
[15] Norcia M A, Kim H, Cairncross W B, *et al.* 2024 *PRX Quantum* **5** 030316
[16] Pichard G, Lim D, Bloch É V J, Bourachot L, Both G J, Mériaux G, Dutartre S, Hostein R, Paris J, Ximenez B, Signoles A, Browaeys A, Lahaye T and Dreon D 2024 *Phys. Rev. Appl.* **22** 024073
[17] Zhang B, Peng P, Paul A and Thompson J D 2024 *Optica* **11** 227
[18] Manetsch H J, Nomura G, Bataille E, Leung K H and Endres M 2025 *Nature* **647** 60
[19] Hill P, Lunt P, Reiter J, Galka M, Preiss P M and Jochim S 2024 *Phys. Rev. A* **110** 053308
[20] Zhao S M, Leach J, Gong L Y, Ding J and Zheng B Y 2012 *Opt. Exp.* **20** 452
[21] Nogrette F, Labuhn H, Ravets S, Barredo D, Béguin L, Vernier A, Lahaye T and Browaeys A 2014 *Phys. Rev. X* **4** 021034
[22] Čižmár T, Mazilu M and Dholakia K 2010 *Nat. Photon.* **4** 388
[23] López-Quesada C, Andilla J and Martín-Badosa E 2009 *Appl. Opt.* **48** 1084
[24] Bowman R W, Wright A J, Padgett and Miles J 2010 *J. Opt.* **12** 124004
[25] Zupancic P, Preiss P M, Ma R, Lukin A, Eric T M, Rispoli M, Islam R and Greiner M 2016 *Opt. Exp.* **24** 13881
[26] Shih C Y, Motlakunta S, Kotibhaskar N, Sajjan M, Hablützel R and Islam R 2021 *npj Quantum Inf.* **7** 57
[27] Yu X, Li H, Sang X, Su X, Gao X, Liu B, Chen D, Wang Y and Yan B 2021 *Opt. Exp.* **29** 11009
[28] Cui S, Wang B and Zheng Q 2023 *Opt. Exp.* **31** 13585
[29] Schmidt K, Guo N, Wang W, Czarske J and Koukourakis N 2023 *Opt. Exp.* **31** 16133
[30] Gutierrez Y, Mazoyer J, Mugnier L M, Herscovici S O and Abeloos B 2024 *Opt. Exp.* **32** 31247
[31] Kim D, Keesling A, Omran A, Levine H, Bernien H, Greiner M, Lukin M D and Englund D R 2019 *Opt. Lett.* **44** 3178
[32] Matsumoto N, Inoue T, Ando T, Takiguchi Y, Ohtake Y and Toyoda H 2012 *Opt. Let.* **37** 3135
[33] Schymik K N, Ximenez B, Bloch E, Dreon D, Signoles A, Nogrette F, Barredo D, Browaeys A and Lahaye T 2022 *Phys. Rev. A* **106** 022611
[34] Chew Y T, Poitrinal M, Tomita T, Kitade S, Mauricio J, Ohmori K and De L S 2024 *Phys. Rev. A* **110** 053518
[35] Wen K, Chen H J, Yan X, Ren Z J, He C D, Hajiyev E, Fung Wong P T, Jo G B 2024 *Chin. Phys. B* **33** 120703
[36] Armstrong D J, Stilgoe A B, Nieminen T A and Rubinsztein D H 2022 *Front. Nanotechnol.* **4** 998656